Title

Characterization of Noise in Parametric Receivers with Electrically Small Antennas

Author

Liu, Yang

Publication Date

2024

Peer reviewed|Thesis/dissertation

UNIVERSITY OF CALIFORNIA

Los Angeles

Characterization of Noise in Parametric Receivers with Electrically Small Antennas

A thesis submitted in partial satisfaction

of the requirements for the degree Master of Science

in Electrical and Computer Engineering

by

Yang Liu

2024

ABSTRACT OF THIS THESIS

Characterization of Noise in Parametric Receivers with Electrically Small Antennas

by

Yang Liu

Master of Science in Electrical and Computer Engineering

University of California, Los Angeles, 2024

Professor Yuanxun Wang, Chair

A direct active matching method with parametric amplifiers to electrically small antennas was previously proposed, which showed its benefits over conventional approaches for its stability and low-noise characteristics. In addition, theoretical derivations were conducted based on this proposed circuit model. In this thesis, an MMIC design of the parametric receiver using the GCS D10 technology is created and simulated to validate the theories. Also, various challenges regarding noise performance come along with the realization of the design. Multiple approaches are presented to counteract environmental noise coming from both signal and pump ports of the parametric amplifier to preserve its intrinsic noise performance.

The thesis of Yang Liu is approved.

Mau-Chung Frank Chang

Aydin Babakhani

Yuanxun Wang, Committee Chair

University of California, Los Angeles

2024

Table of Contents

List of Figures

Acknowledgment

I want to thank my supervisor, Professor Yuanxun Wang, for his professional guidance, remarks, and support for this work. Professor Wang is always encouraging and thoughtfully guiding our academic progress. During my journey pursuing the master's degree, I can recall many times when I felt lost and not confident about my work, but with Prof. Wang's encouragement and detailed derivation in his research, I was able to regain insights into my topic. Professor Wang always worked himself to his best, and he really motivated and showed me what qualities an actual professional in the field needs to embody.

Additionally, I would like to thank Professor M. C. Frank Chang, and Professor Aydin Babakhani for their patience in reading and approving this work.

I am truly grateful to my lab mates and friends, Lap Yeung, Nancy Gao, Sean Chen, Ben Huang, Kamal Bhakta, Josh Yu, Alice Yang, Selina Pan, and Anna Wang, for their professional guidance, heartwarming help, and inspiring discussions during the past few years.

A huge thanks to Mr. Hsu, Mr. Koyfman, and Ms. Zhang. You all have taught me in class for academic materials and out of class for life lessons. As mentors and teachers, you lovingly took me in, protected, and guided me even when I wasn't in my best condition, and more importantly, you witnessed how much I've grown over the past years.

I would also like to thank my family for their unconditional love. Starting with my brothers Allen and Max for always being there, listening to my thoughts, and comforting me, and my parents for loving me no matter who I've become. Without of their support, I wouldn't be able to make it through the end of this journey.

CHAPTER 1

Introduction

The gain-bandwidth limitations and noise challenges have long limited the performance in electrically small antennas (ESAs). Many studies focused on ways to overcome this limitation, and among them, the previously proposed method of direct active matching of parametric devices to ESAs embodies good gain and low noise performance while avoiding extra noise introduced by any impedance matching network.

1.1 Background and Motivation

Electrically small antenna applications (ESA) are widely used in VHF and UHF for wireless communications for their small form factor compared to the long wavelength of electromagnetic (EM) waves within the frequency range. In practice, an electrically small antenna is any antenna operating below its natural resonance frequency. However, despite the benefits that come along with their sizes, ESAs also comply with the restrictions introduced by their electrical size. As it is defined by Chu and Harrington [3], the lower bound of the Q_{rad} is stated as following:

$$Q = \frac{1}{(ka)^3}, where\ ka \ll 1 \tag{1.1.1}$$

Where k is the wavenumber in free space and the radius of the smallest surrounding sphere that can contain the whole aperture. To maximize antenna gain, it is crucial to minimize the radiation Q factor. This is due to the direct relationship between radiation efficiency and the radiation Q factor; as the radiation Q decreases, the radiation efficiency correspondingly increases, with the knowledge that $Q_{material} \ll Q_{rad}$ [3].

$$E_{rad} = \frac{P_{rad}}{P_{rad}+P_{loss}} = \frac{\frac{W}{Q_{rad}}}{\frac{W}{Q_{rad}}+\frac{W}{Q_{material}}} = \frac{Q_{material}}{Q_{rad}+Q_{material}} \approx \frac{Q_{material}}{Q_{rad}} \quad (1.1.2)$$

In addition, the Bode-Fano limit indicates that energy delivery efficiency and bandwidth product of a high-Q load is subject to the relation shown in equation (1.1.3), demonstrating the tradeoff between efficiency and bandwidth bounded by the radiation Q. Hence, maintaining the radiation Q at its minimum value is imperative for achieving optimal antenna performance.

$$\eta * B < \frac{1}{Q_{rad}} \quad (1.1.3)$$

More importantly, for receivers, the Shannon-Hartley theorem states,

$$C = Blog_2\left(1+\frac{S}{N}\right) \quad (1.1.4)$$

Where C is the channel capacity in bits per second, B is the bandwidth of the channel in Hz, S is the average received signal power over the bandwidth, and N is the average power of the noise and interference over the bandwidth. The theorem shows that with a lower average noise power, the SNR increases, leading to an increase in the theoretical upper bound of the information rate of data that can be communicated at an arbitrarily low error rate. With that in mind, novel matching techniques and designs are made to overcome this bandwidth-SNR conundrum. The noise figure of the parametric receiver is evaluated with the GCS D10 diode technology under different matching techniques. With the direct matching option from antenna to parametric amplifier, both

the noise figure and noise matching bandwidth can be vastly improved compared to conventional impedance-matched cases.

1.2 Traditional Impedance Matching Network

The traditional matching methods include transmission line matching and lumped component matching. These external matching networks have their pros and cons. For transmission line matching, it typically has a better Q compared to the lumped components. However, since transmission lines' electrical lengths highly depend on the wavelength, which varies with the frequency, the transmission line matching method usually has a narrow bandwidth. Conversely, the lumped component matching method can have a much broader bandwidth, but the low Q characteristics degrade the SNR in exchange for the benefit. Y. Wang et al. proposed the following equivalent circuit to quantify the NF and SNR of the indirect matching circuit [1].

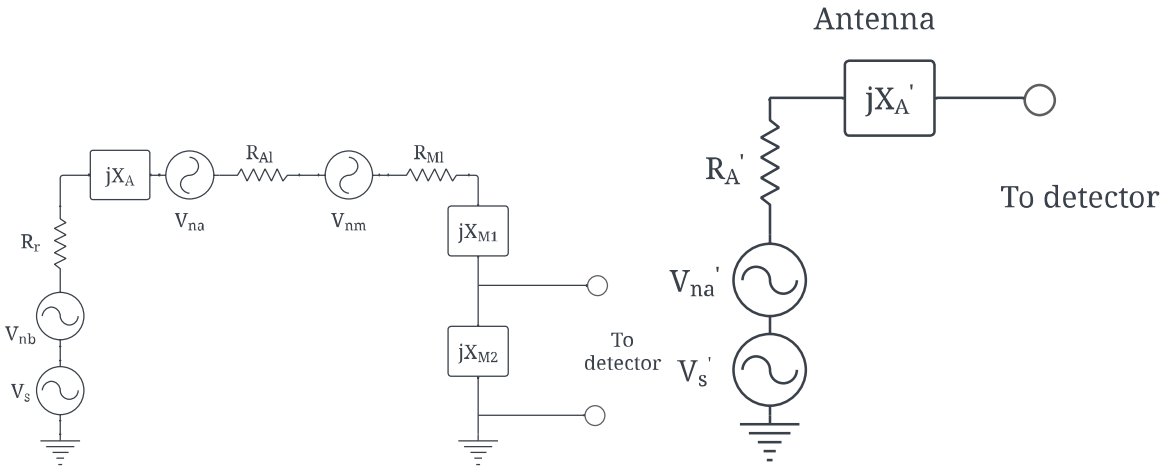

Figure 1.2.1 (a) Circuit diagram of conventional matching networks, (b) The simplified circuit

In Figure 1.2.1, the equivalent circuit model from the antenna end to the detector input is provided above. The voltage sources V_{na}, V_{nb}, V_{nm} denote the noise from unmatched antenna due to loss, the background noise, and the noise due to the matching network, respectively. R_a is the antenna radiation resistance. R_{Al} represents the loss of the antenna and R_{Ml} represents the loss of the matching network. X_A denotes the unmatched antenna reactance and X_{M1} and X_{M2} are the reactance of the matching network that not only resonates with the antenna, but also transforms the antenna impedance.

With the extra impedance matching network, the impedance transformation is calculated below [1]:

$$R'_A + jX'_A = \frac{jX_{M2}(R_r + R_{Al} + R_{Ml} + jX_A + jX_{M1})}{R_r + R_{Al} + R_{Ml} + jX_A + jX_{M1} + jX_{M2}} \tag{1.2.1}$$

At resonance,

$$X_A + X_{M1} + X_{M2} = 0 \tag{1.2.2}$$

The characteristic impedance Z_0 is conventionally chosen to be 50Ω,

$$R'_A(\omega_r) = \frac{X_{M2}^2}{R_a + R_{Al} + R_{Ml}} \tag{1.2.3}$$

Thus, the impedance is also transformed to 50Ω. The following equation is used to calculate the noise figure of the matched antenna-detector pair:

$$NF_d(\omega_r) = 10\, log_{10}\left[1 + \frac{R_g}{R'_A(\omega_r)}\right] \tag{1.2.4}$$

Next, we need to calculate the SNR; the signal-to-noise ratio (SNR) of the incident wave is defined at the wave port as the ratio of the power density of the electromagnetic waves from the transmitter arriving at the antenna input to that of the background thermal emission. The received signal power can be described as:

$$V_s = \sqrt{4S_0R_a} \tag{1.2.5}$$

In the equation, S_0 is the maximum achievable signal power received by the antenna is considered under the condition where antenna loss and matching network loss are absent. It is important to note that Figure 1.2.1 assumes a series configuration of various noise sources and the signal source. This configuration implies that the radiated power, Ohmic loss of the antenna, and Ohmic loss of the matching network are proportional to the square of a common current flowing through the antenna port. Here, the antenna loss and matching network loss are represented by the Ohmic resistances of the wires and the matching element.

For other types of ESAs, such as those incorporating dielectric materials or more sophisticated matching networks, a combined series and parallel circuit model may be utilized. In such a model, the resistances are transformed into composite versions of the originally defined radiation resistance, Ohmic resistances, and dielectric losses. Despite these transformations, a similar noise analysis remains applicable.

The SNR at the input is defined as:

$$SNR_i = \frac{V_s^2}{V_{nb}^2} = \frac{S_0}{N_0} \tag{1.2.6}$$

The SNR at the output is defined as:

$$SNR_0 = \frac{d^2 V_S^2}{d^2(V_{nb}^2 + V_{na}^2 + V_{nm}^2)} = \frac{\frac{R_a}{R_a + R_{Al} + R_{Ml}} * S_0}{N_0} = \frac{\eta S_0}{N_0} = \eta SNR_i \quad (1.2.7)$$

$$NF_A = \frac{SNR_i}{SNR_o} = \frac{1}{\eta} = \frac{R_a + R_{Al} + R_{Ml}}{R_a} \quad (1.2.8)$$

The noise figure of the antenna is represented as a degradation of the overall SNR, which leads to the conclusion that the loss of the additional matching network degrades the SNR performance of the receiver.

1.3 Direct Matching Techniques

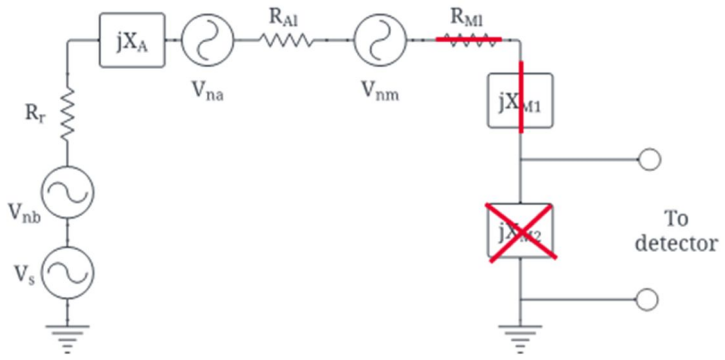

Fig 1.3.1 Circuit diagram for direct matching

Two direct matching techniques are discussed in this section: field fet matching and direct matching with a parametric amplifier. In the article from Y. Wang et al., he proposed two equivalent circuit models and analysis to compare these two options [1].

For the direct active noise matching with the transistor option,

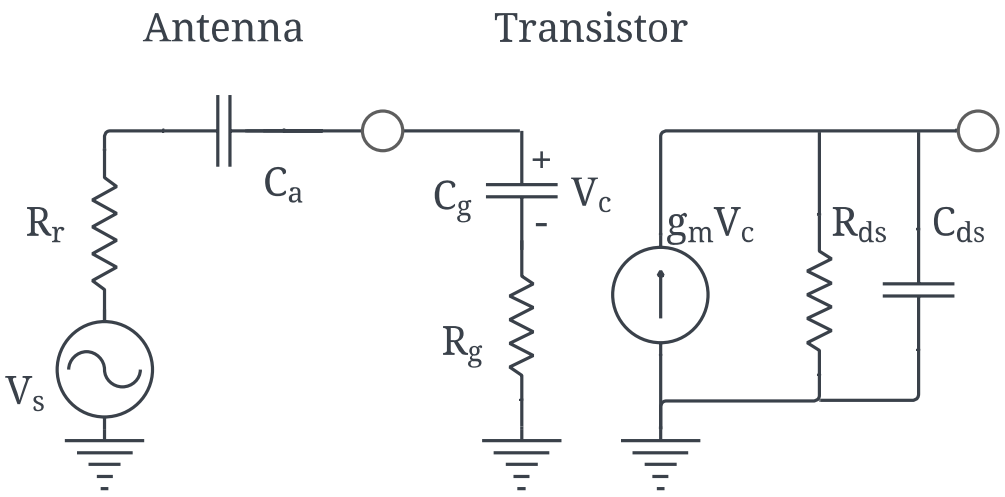

Fig 1.3.2 Circuit diagram of direct active matching with transistor

At the output of the transistor, the open circuit voltage at the drain is yielded as following:

$$V_{ds}^2 = (g_m V_{cs} R_{ds})^2 = 8S_0 \left(\frac{g_m}{\omega C_g}\right)^2 \frac{R_r R_{ds}^2}{\left(R_r + R_g\right)^2} \tag{1.3.1}$$

Under the conjugate output match condition ($R_l = R_{ds}$), the transducer gain becomes:

$$G_T = \frac{V_{ds}^2}{R_l} * \frac{1}{S_0} = \left(\frac{g_m}{\omega C_g}\right)^2 \frac{R_r R_{ds}}{\left(R_r + R_g\right)^2} \tag{1.3.2}$$

The optimum noise figure is, thus,

$$F_{N,T} = \frac{SNR_{in}}{SNR_{out}} = \frac{S_0}{N_0}\frac{V_{dn}^2}{V_{ds}^2} = \frac{R_r + R_g}{R_r} + \left(\frac{\omega C_g}{g_m}\right)^2 \frac{\left(R_r + R_g\right)^2}{R_r R_{ch}} = 1 + \frac{R_i}{R_s} + \frac{1}{G_T}\frac{R_{ds}}{R_{ch}} \tag{1.3.3}$$

With the direct matching situation, it presents us with the benefit of simplicity, and it also offers us a wide bandwidth. However, this technique requires a large periphery of transistors (shunt

transistors) to reduce gate resistance, better noise figure and bandwidth. As a result, it also incurs more power consumption.

Then, we would like to discuss the direct active matching with parametric amplifiers [9]:

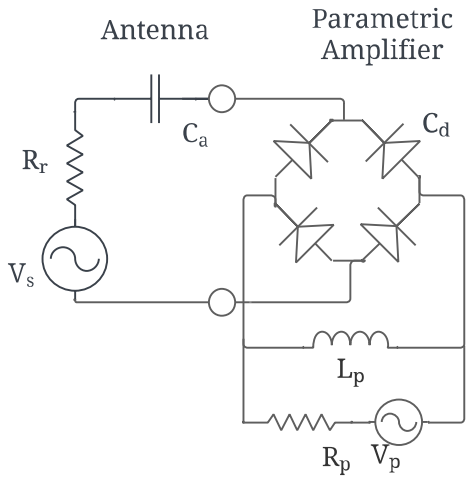

Fig 1.3.3 Circuit diagram for direct active matching with parametric amplifier

In Figure 1.3.3, the circuit diagram is provided for direct active matching with parametric amplifier with R_r and C_a being the equivalent circuit of the antenna, and the diode bridge composed of four identical diodes with a capacitance of C_d. L_p is the inductance of the resonating inductor at the pump. R_p and V_p combined are the pump source to the parametric amplifier. R_p is conventionally 50Ω for input-matched RF circuits.

The equivalent circuit diagram is presented above, and the transducer gain is:

$$G_T = \frac{Y_0 G_s}{(Q_a Y_0 + Q_d G_s)^2} Q_d^2 \gamma^2 \tag{1.3.4}$$

For an optimum result, we need to maximize the transducer gain,

$$Q_a Y_0 = Q_d G_s \tag{1.3.5}$$

$$C_a = C_d \tag{1.3.6}$$

The maximized single sideband transducer gain is, thus,

$$G_{T,max} = \frac{1}{4}\frac{Q_d}{Q_a}\gamma^2 \tag{1.3.7}$$

Here Q_d and Q_a are the diode quality factor and the antenna quality factor, respectively,

For the double sideband situation, the maximized transducer gain also becomes doubled:

$$G_{T,max} = \frac{1}{2}\frac{Q_d}{Q_a}\gamma^2 \tag{1.3.8}$$

Eventually, we land at the noise figure calculation:

$$F_{N,P} = 1 + \frac{G_s}{Y_0} + \frac{1}{G_{T,max}} = 1 + \frac{Q_a}{Q_d}\left(1 + \frac{2}{\gamma^2}\right) \tag{1.3.9}$$

In summary, after comparing the two techniques, we can conclude that the field fets typically have higher transducer gain while parametric amplifiers are more stable. For similar technologies, $Q_g \ll Q_d$ due to coupling of the gate to the channel through Miller capacitance. This implies parametric amplifiers can realize lower noise figure, if a positive transducer gain can be achieved. For power consumption considerations, parametric amplifiers are much more efficient than three-terminal devices since they don't need to be cascaded to shrink the gate resistance.

1.4 Thesis Outline

In this thesis, the parametric receiver chain is broken down into the antenna part and the amplifier part, where each chapter discusses the fundamental principle of each device and then analyzes the noise contribution of every component. In Chapter 2, the circuit model of bowtie antennas is

reviewed, and how its performance can be quantified is discussed in the sections. In Chapter 3, the fundamental principles of parametric amplification are described, and the chapter focuses on the design and simulation of the MMIC parametric receiver design. The results are presented and compared to the results from preceding theorems. Subsequently, Chapter 4 characterizes and counteracts the noise factors that would contribute to the noise performance of the receiver chain. Finally, Chapter 5 discusses the future work of this application and concludes the thesis.

CHAPTER 2

Bowtie Antenna Characteristics

2.1 Bowtie Antenna Chu's equivalent circuit

To establish a feasible approach for analyses and simulations of the receiver gain and noise figure that is derived from the output of the antenna to the input of the parametric amplifier, a close study of a circuit model from S-parameters obtained from full-wave simulation software, such as HFSS, and CST Studio so that pseudo noise sources and source resistances can be accounted for in the results, Chu's original paper derived the Chu's limit based on his circuit model for the lowest order electric dipole and magnetic dipole as shown in the figure 2.1.1 below [3].

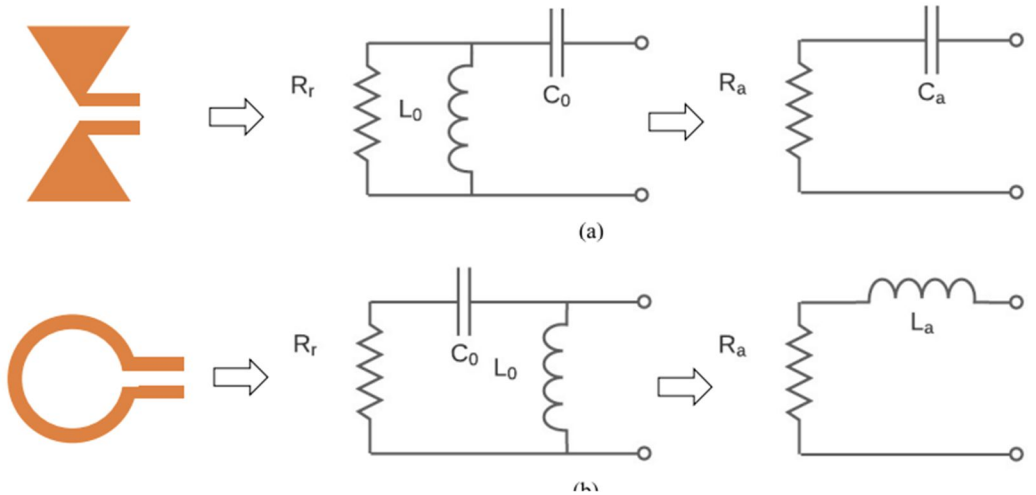

Fig 2.1.1 (a) Equivalent circuit model of the electrically small dipole for $\mathbf{TM_1}$ mode and its simplified version under high Q assumption, (b) Equivalent circuit model of the electrically small loop for $\mathbf{TE_1}$ mode and its simplified version under high Q assumption.

According to Chu's paper, the lowest order mode for electric dipole (TM_1) and magnetic dipole (TE_1) are analyzed and converted into their equivalent circuits via R, L, C components to represent the real and imaginary part of the scattering parameter. The circuits capture the exact performance of the antennas up to their first resonance and illustrate the near-field energy characteristics of both modes outside the minimum size sphere that encloses the aperture. In the paper from Y. Wang et al., a close analysis of the radiation quality factor extracted from the equivalent circuits is presented. L_0 and C_0 values are characterized by the following equations to the radiation resistance R_r, and they are closely bounded by the radius of the sphere and the speed of light c[1].

$$\begin{cases} L_0 = \dfrac{a}{c} R_r \\ C_0 = \dfrac{a}{cR_r} \end{cases} \tag{2.1.1}$$

To simplify the circuit model, the high-Q assumption is adopted (ESA characteristic). Now, the circuit model for the dipole and loop antenna can be further represented as a series RL or RC circuit, shown in Figure 2.1.1. The values are calculated using the expressions below [1]:

$$\begin{cases} R_a \approx \dfrac{(\omega L_0)^2}{R_r}, \quad C_a \approx \dfrac{C_0}{1-\omega^2 L_0 C_0} \approx C_0 \\ R_a \approx \omega^4 L_0^2 C_0^2 R_r, \quad L_a \approx \dfrac{L_0}{1-\omega^2 L_0 C_0} \approx L_0 \end{cases} \tag{2.1.2}$$

2.2 Antenna Radiation Quality Factor

After retrieving the antenna equivalent circuit model, Y. Wang et al. also proved a way to calculate the antenna's radiation quality factor [1]. While we revisit the simplified circuit shown in Figure 2.1.1, we can perceive that unlike C_a, L_a which remains almost constant when the frequency is far

below the first resonance frequency, the radiation resistance is now highly frequency-dependent with them being either second or fourth order of the frequency respectively. The radiation quality factor is calculated below [1]:

$$\begin{cases} Q_a = \dfrac{1}{\omega C_a R_a} \approx \dfrac{R_r}{\omega^3 L_0^2 C_0} \ (electrically\ small\ dipole) \\ Q_a = \dfrac{\omega L_a}{R_a} = \dfrac{\omega L_0}{\omega^4 L_0^2 C_0^2 R_r} \approx \dfrac{1}{\omega^3 L_0 C_0^2 R_r} \ (electrically\ small\ loop) \end{cases} \tag{2.2.1}$$

The antenna quality factor is used in the latter calculation of the gain and noise figure of the whole parametric receiver chain.

CHAPTER 3

Parametric Amplification Simulation and Prototypes

3.1 Background of Parametric Amplification

The Manley-Rowe relation is derived from the general principle of energy conservation and relates the powers at different frequencies in a nonlinear reactor modulator [10]. The relation stays valid for all signal levels (small and large signal level) as long as the lossless condition holds. It describes harmonics, intermodulation, and the energy transfer mechanism among different tones under different termination conditions. In figure 3.1.1, it shows Manley and Rowe's equivalent circuit with two voltage sources at $\omega_1$and ω_2. The sources and an infinite array of resistive loads and bandpass filters are placed across the nonlinear capacitor. The resistor-filter pairs are tuned to the frequencies of $n\omega_1 + m\omega_2, with\ n, m$ as integers ranging from 0 to infinity [10]. The Manley-Rowe relation satisfies all three modes of parametric amplification introduced next based on the termination of intermodulation tones and harmonics.

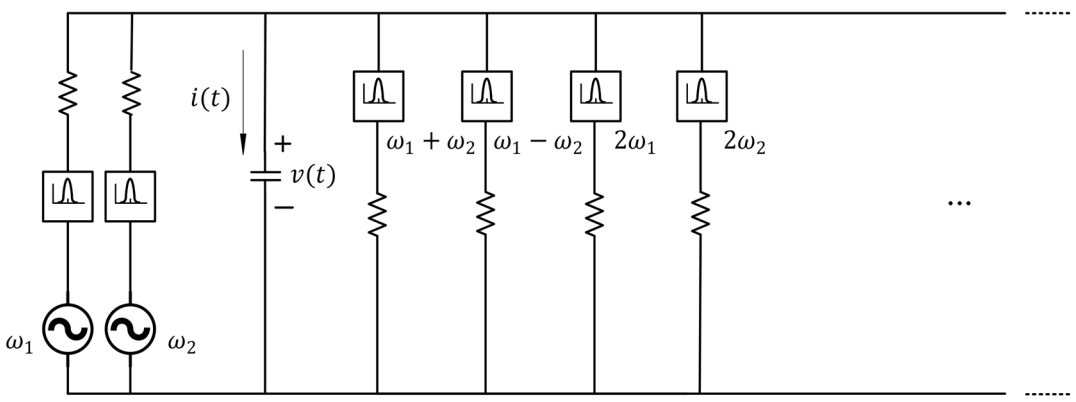

Fig 3.1.1 Circuit model for Manley-Rowe derivation

To begin with, for negative resistance mode, only strong current sources that are permitted to exist are at the signal, pump, and idler.

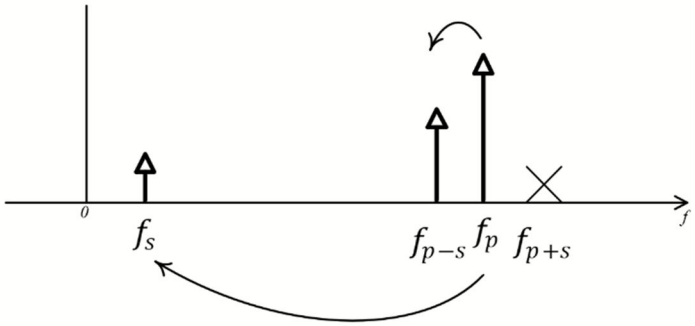

Fig 3.1.2 Negative resistance mode

The power flow relation can be summarized as:

$$\frac{P_{p-s}}{P_s} = \frac{\omega_{p-s}}{\omega_s} \tag{3.2.1}$$

For single sideband upconverting mode, the only strong voltage sources are at the signal, pump, and idler. However, unlike the double sideband upconverting mode, this mode only has one output at the idler frequency, which is located at the sum of the pump and the signal frequency. The power flow relation is summarized as following:

$$\frac{P_{p+s}}{P_s} = -\frac{\omega_{p+s}}{\omega_s} \tag{3.2.2}$$

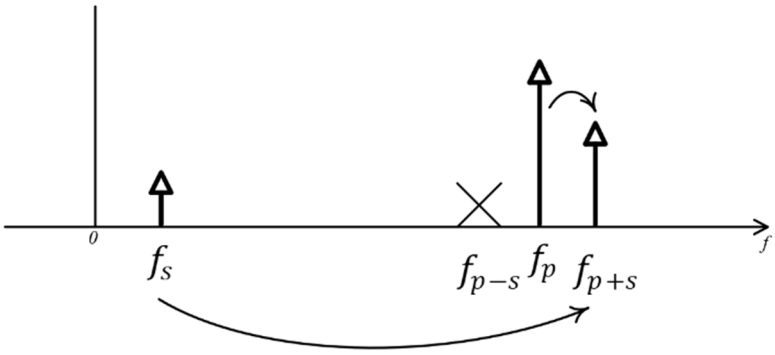

Fig 3.1.3 Single sideband upconverting mode

For the double sideband up-converting mode, it needs to satisfy the following two conditions: the only strong voltage present in the system are the input (signal), output (idler), and pump frequency, as well as the output of the amplifier, needs to be the sum and difference of the input and the pump frequency for double sideband case:

$$f_i = f_p \pm f_s \tag{3.2.3}$$

The power flow relations can be summarized as:

$$\frac{P_{p+s}}{P_p} = -\frac{\omega_{p+s}}{\omega_p} \tag{3.2.4}$$

$$\frac{P_{p-s}}{P_p} = -\frac{\omega_{p-s}}{\omega_p} \tag{3.2.5}$$

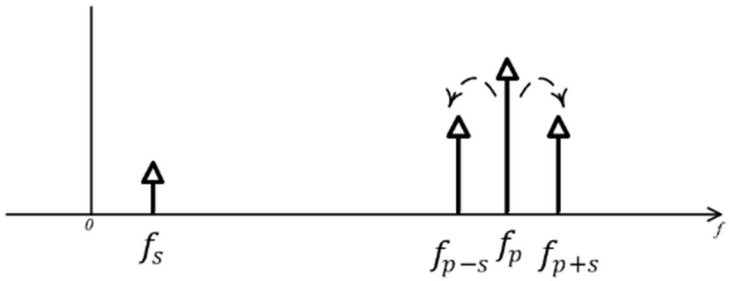

Fig 3.1.4 Double sideband upconverting mode

3.2 Double sideband Up-conversion Parametric Amplifier Gain and NF Calculation

In this work, the double sideband up-converting mode is focused on top of general parametric amplifier behaviors, as the parametric amplification pump either nonlinear reactance via the strong RF pump power to produce either mixed signals with gain or to generate a negative resistance. The previous section introduced the two essential conditions that double sideband up-conversion needs. With these conditions satisfied, the small signal method of Manley-Rowe relations become applicable, and the equivalent circuit is shown below. According to Hedayati, M.'s analysis of the circuit [2]:

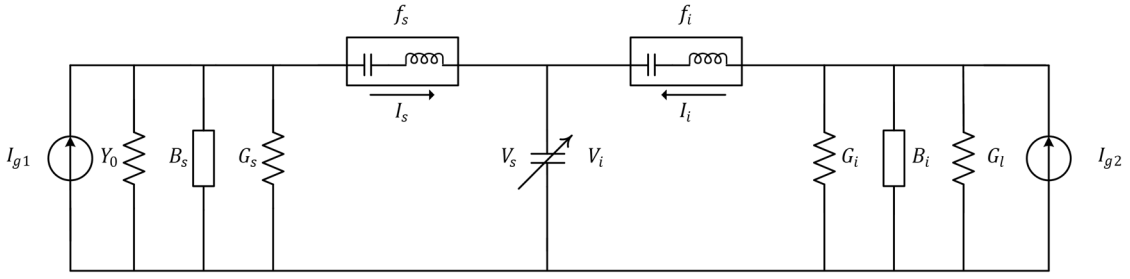

Fig 3.2.1 Simplified circuit model for parametric amplifier

The $C_0\ and\ L_s$ are the mean values of the time-domain capacitance and input resonator, respectively. In the output circuit $C_0\ and\ L_i$ are the output resonators at idler frequency. $G_L, G_i, and\ G_s$ represent output load, the resonator loss at idler, and the resonator loss at signal frequencies, respectively.

A small signal admittance matrix can be therefore obtained [2]:

$$\begin{pmatrix} I_s \\ I_{i-}^* \\ I_{i+} \end{pmatrix} = \begin{pmatrix} Y_{11} & Y_{12} & Y_{13} \\ Y_{21} & Y_{22} & Y_{23} \\ Y_{31} & Y_{32} & Y_{33} \end{pmatrix} \begin{pmatrix} V_s \\ V_{i-}^* \\ V_{i-} \end{pmatrix} = \begin{pmatrix} j\omega_s C_0 & j\omega_s \gamma C_0 & j\omega_s \gamma C_0 \\ -j\omega_{i-} \gamma C_0 & -j\omega_{i-} C_o & 0 \\ j\omega_{i+} \gamma C_0 & 0 & j\omega_{i+} C_0 \end{pmatrix} \begin{pmatrix} V_s \\ V_{i-}^* \\ V_{i+} \end{pmatrix} \tag{3.2.1}$$

Here γ is the capacitance modulation index [2].

$$\gamma \approx \frac{C_{max} - C_{min}}{\frac{C_{max} + C_{min}}{2}} \tag{3.2.2}$$

Where $C_{max}\ and\ C_{min}$ are the maximum and minimum capacitance values caused by the swing of the pump voltage. From Hedayati, M.'s detailed derivation and including the effect of the quality factor of the resonating inductor introduced in Chapter 1, we can conclude [2]:

$$G_{T,max} = \frac{1}{4} \frac{Q_{ind}}{Q_a} \frac{\omega_i}{\omega_s} \gamma^2 \tag{3.2.3}$$

For double sidebands, it becomes,

$$G_{T,max} = \frac{1}{2} \frac{Q_{ind}}{Q_a} \frac{\omega_i}{\omega_s} \gamma^2 \tag{3.2.4}$$

The noise figure is defined as following:

$$F_N = 1 + \frac{G_s}{Y_0} + \frac{1}{G_T} = 1 + \frac{Q_a}{Q_d} + \frac{Q_a}{Q_{ind}} \frac{\omega_s}{\omega_i} \frac{2}{\gamma^2} \tag{3.2.5}$$

3.3 Varactor Diode Modeling with Noise Consideration in Simulations

A varactor diode is designed to produce a strong variation in capacitive reactance with minimal parasitic series resistance, which causes energy dissipation in the system. Leveraging on the rapidly advancing electronics and IC technologies, the minimal series resistance almost becomes the only loss mechanism in varactor diodes. However, extra diode noise characterization is still needed based on the foundry-provided models to serve as a realistic model for the construction of the parametric amplifier.

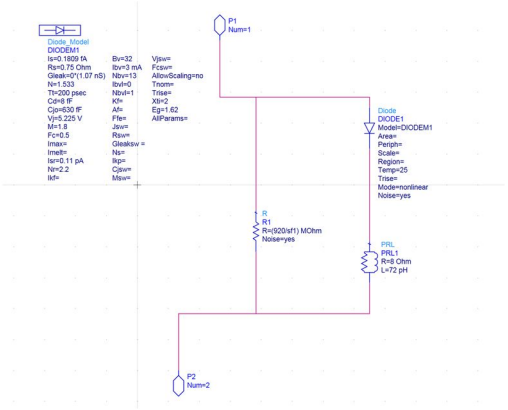

Fig 3.3.1 Diode noise model with shunt conductance

In Figure 3.3.1, the equivalent noise model of the foundry-provided diode is shown. The original Keysight PN junction diode model also overpredicted shot noise in the reverse biasing condition. It considered the entire leakage current, either from the channel or from the material loss, as the source of shot noise. We can now separate the DC and RF path by shunting a large value resistor to the diode. The shunt resistance dominates at lower frequencies, and the resistance can be ignored at higher frequencies. Now, the diode noise model can accurately illustrate the noise introduced by

the diode. All other specifications remain identical to the ones provided in the PDK. Multiple diodes are shunted together to form one “super” diode with the desired capacitance. The number of diodes is calculated based on the ratio of total capacitance needed to resonate with the antenna to the single diode equivalent capacitance. In our case, a total of 30 diodes are shunted together to construct each of the four diode representations in Figure 3.3.5. In addition, a distribution network is added to avoid phase delays while simultaneously exciting numbers of diodes.

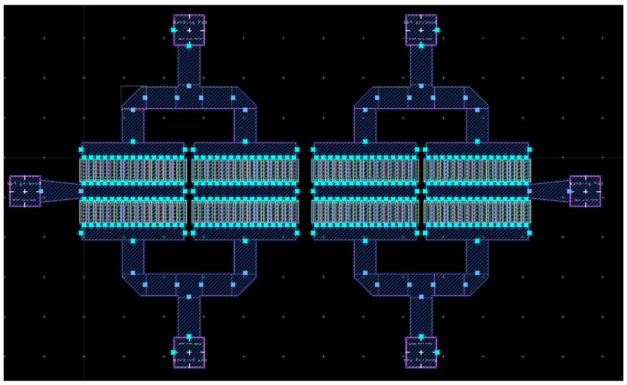

Fig 3.3.2 Differential diode bridge design with distributed network at the pump port

Figure 3.3.2 shows an MMIC design of the diode bridges with differential input. The diodes are from the GCS InGaAs HBT D10 process. 30 diodes are distributed evenly to each arm of the distribution network. The diode bridge characteristics are simulated and captured using ADS EM simulation. An adaptive sweep from DC to 4 GHz is adopted for the simulation.

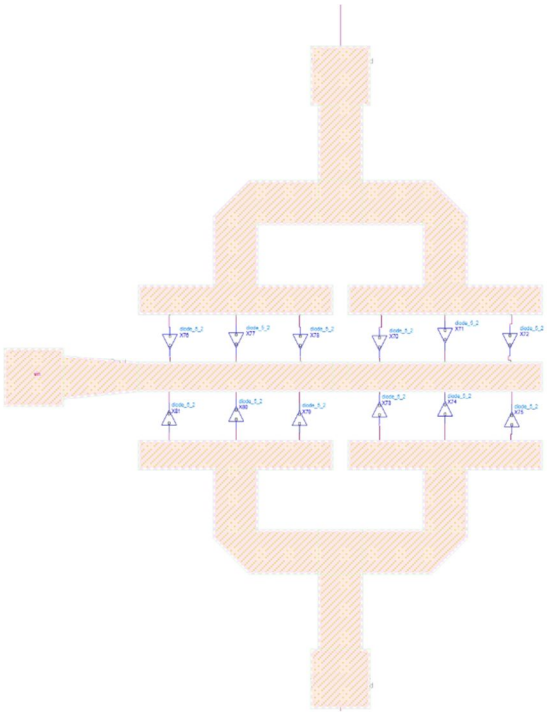

Fig 3.3.3 Zoomed in view of the diode bridge schematics

In Figure 3.3.3, a zoomed-in view of the diode bridge schematics is presented, with three “super” diodes spaced evenly on each arm of the distribution network. Such a design is intended to have all diodes excited simultaneously so that the signals through the diode bridge are not distorted due to any possible phase delay.

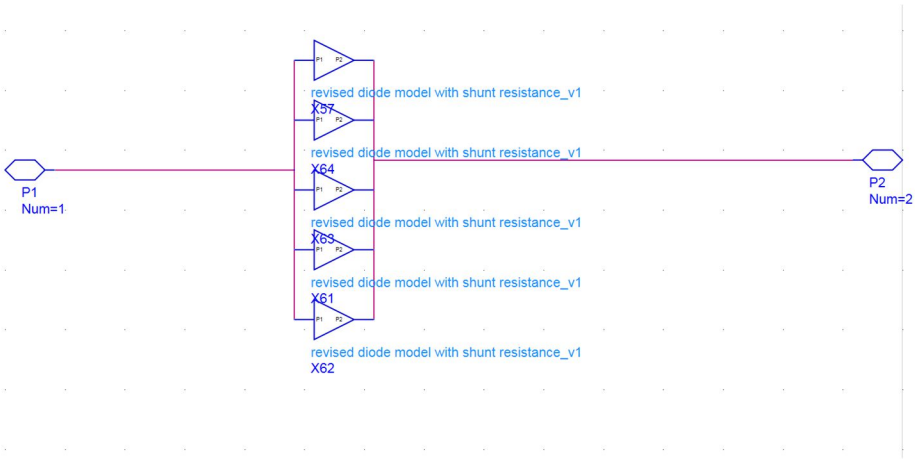

Fig 3.3.4 "Super" diode construction

In Figure 3.3.4, multiple diodes, as shown in Figure 3.3.1, are connected in parallel to form a "super" diode. The number of diodes is determined by half of the total number of diodes divided by the number of pins we assign to each arm of the distribution network. In this project, the total number of diodes is determined by the total mean capacitance needed to resonate with the antenna divided by the capacitance value of the diode under a certain reversed bias voltage. This relation yields a total number of 30 diodes for each side of the diode bridge, and these diodes are equally divided into two by the distribution network. With three pins on each arm of the distribution network, the "super" diode is therefore constructed with five diodes connected in parallel.

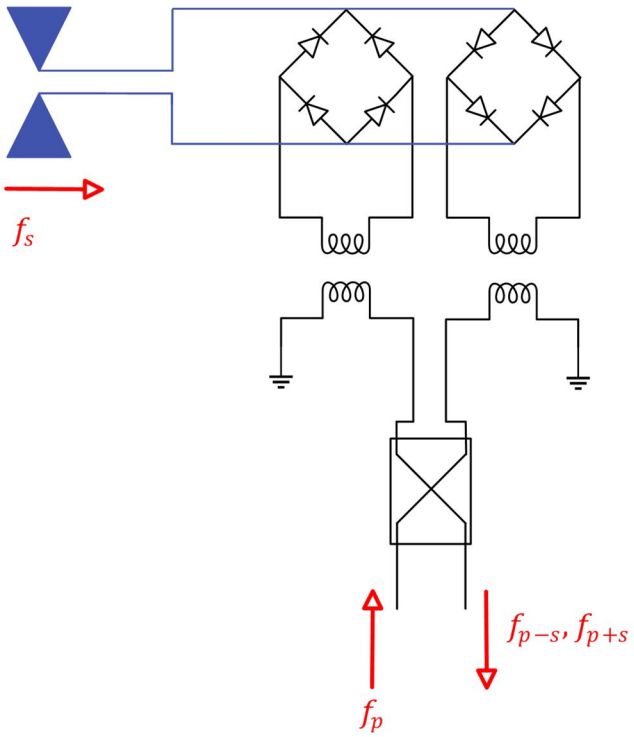

Fig 3.3.5 Schematic level parametric receiver chain

In Figure 3.3.5, the whole parametric receiver chain is presented again with the antenna, parametric amplifier, baluns, and circulator/coupler for a high-level overview. By providing the diode bridges with strong pump power, the upconverted signals are amplified and down converted to the original input frequency so the two sidebands combine, and the noise figure can be defined for the same input and output frequency. The simulation results are detailed in the next section.

3.4 Preliminary simulation results for the parametric receiver with off-chip components

To verify the theories above, we must construct the receiver and run the simulations in ADS to verify the consistency between theoretical and simulation results. Firstly, the resonance of the parametric amplifier needs to be validated.

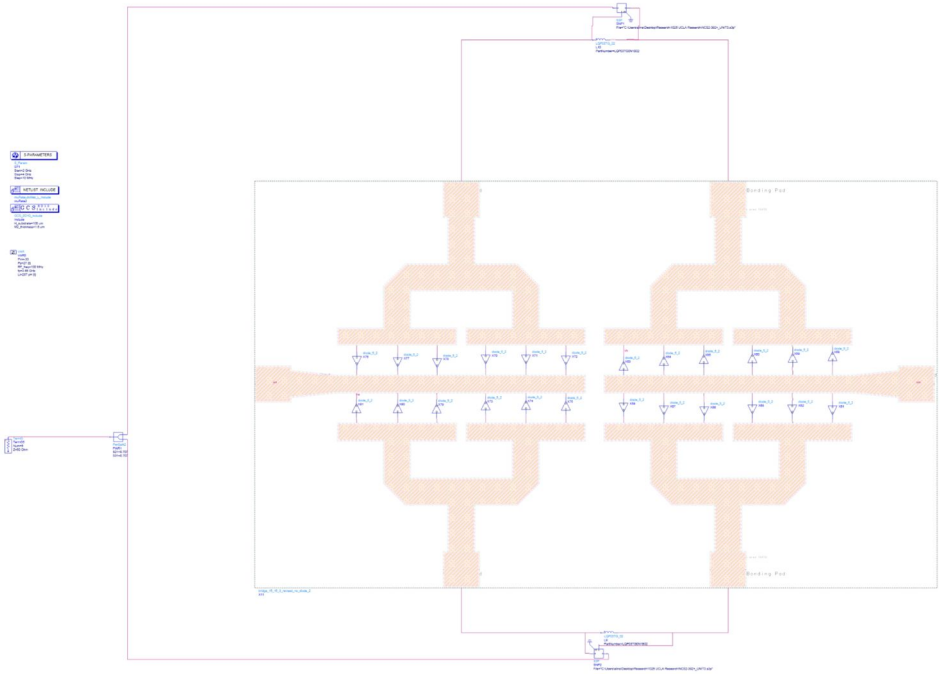

Fig 3.4.1 Schematic of S-parameter measurement from the pump port

In Figure 3.4.1, the circuit is set up for the S-parameter measurement through the pump port. It is expected that the resonance appearing at intrinsic pump frequency will be shown through small signal analysis. Murata inductor LQP03TG0N1B02 with an inductance of 0.1 nH is used to resonate with the diode bridge. The balun utilizes the LTCC RF transformer with low insertion

loss under 0.05 dB and wide bandwidth ranging from 3000 to 3900 MHz. An ideal power divider is used to power the pump sources simultaneously. The simulation runs from 2 GHz to 4 GHz with a step-size of 10 MHz, and the result is shown below. The pump bias is set to be 4.1V.

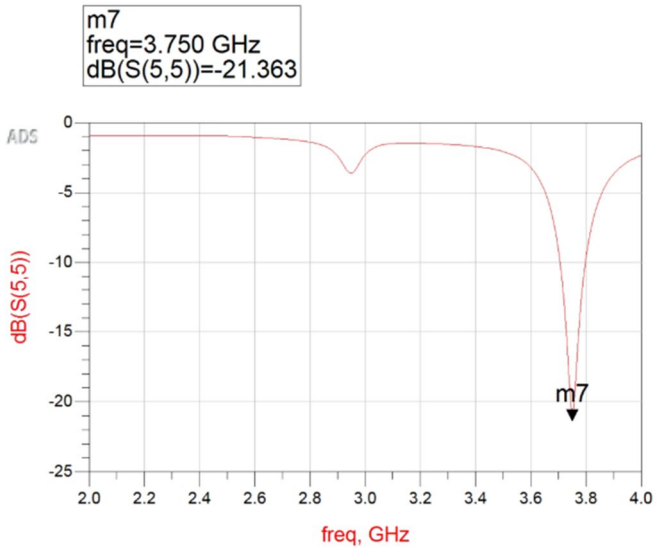

Fig 3.4.2 S-parameter result from the pump port

In Figure 3.4.2, the S-parameter result is presented, and the resonance is spotted at 3.75 GHz with our desired large signal pump frequency at $f_p = 3.65\ GHz$. The phenomenon is because, in large signal cases, the strong pump power modifies the nonlinear reactance, increasing the diode capacitance, and thus, the resultant pump frequency decreases. With that in mind, the S-parameter result shows consistency to our expectations. Then, we would move to the large signal analysis using the harmonic balance analysis of ADS. In the controller, we would like to set the maximum mixing order to a high value of 4 in order to account for the termination of higher orders of intermodulation that is essential to parametric amplifier performance and set RF frequency (signal) sweep to range from 10 MHz to 120 MHz with a step size of 2 MHz.

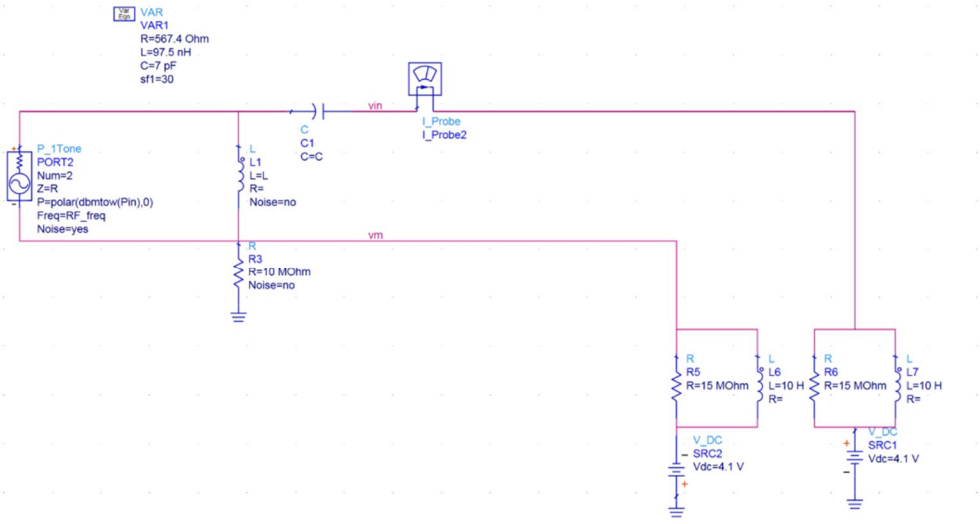

Fig 3.4.3 Schematic of the signal input through a circuit mockup of the antenna.

In Figure 3.4.3, the circuit of the signal input of the parametric amplifier is shown. The AC signal input is defined at the RF frequency sweeping from 10 MHz to 120 MHz. The shunt pair of 15 $MOhm$ resistor and $10H$ inductor serves to isolate the DC and RF paths. At low frequency, the inductance dominates (short circuit), and at high frequency, the resistance dominates (open circuit). An equivalent RLC circuit is extracted for the dipole antenna with $ka = \frac{1}{2}$, and the bowtie antenna is shown in the figure 3.4.4. The antenna is designed with a maximum radius of 238 mm. The S-parameter is simulated and extrapolated from ADS and fitted to Chu's equivalent electrically small dipole model for TM_1 mode introduced in Chapter 2. The extracted R, L, C values are 567.4Ω, 97.5 nH, and 7 pF respectively. The PCB level parametric amplifier indicating the physical location where the device is directly matched to the antenna is shown on the top of the antenna model. The v_{in} and v_m pins are connected to the antenna inputs of the parametric amplifier respectively in figure 3.4.2.

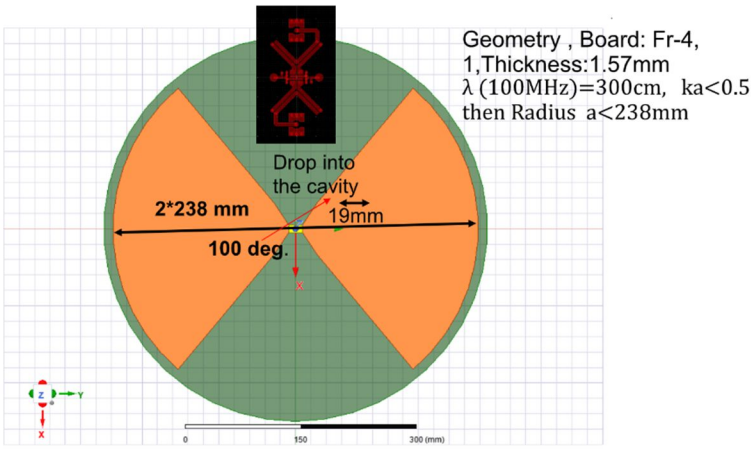

Fig 3.4.4 Bowtie antenna with ka =1/2,

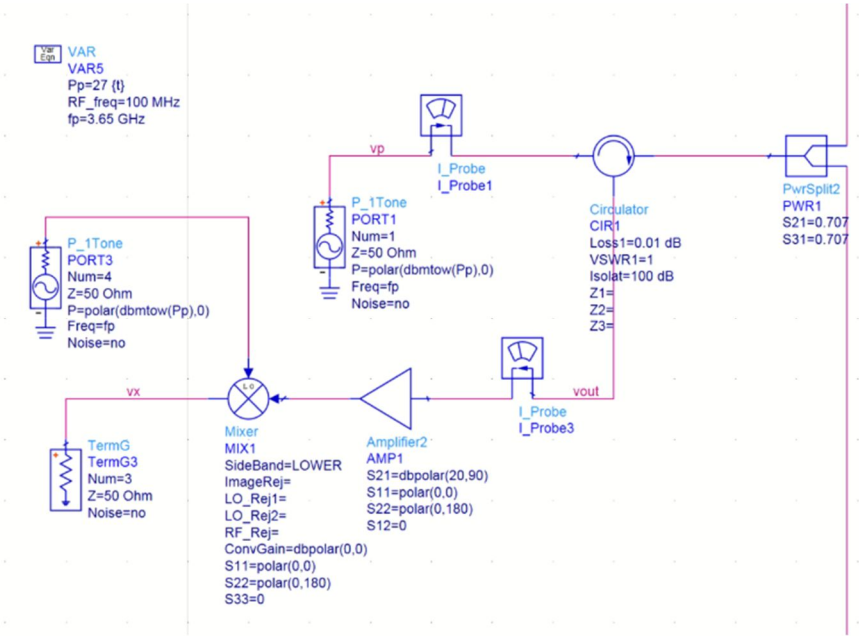

Fig 3.4.5 Pump and idler circuitry

In Figure 3.4.5, the pump port of the parametric amplifier is shown. The pump power is set to be 27 dBm, and the pump frequency f_p at 3.65 GHz. The circulator loss factor is set to be 0.01 dB, and the ideal isolation of 100 dB is provided between the pump circuitry and the idler circuitry. An

ideal power divider is used for equally splitting the pump power between the two baluns, as shown in Figure 3.4.1. The upconverted idler signals are further amplified and downconverted through the LNA and mixer to avoid leakage from the pump noise.

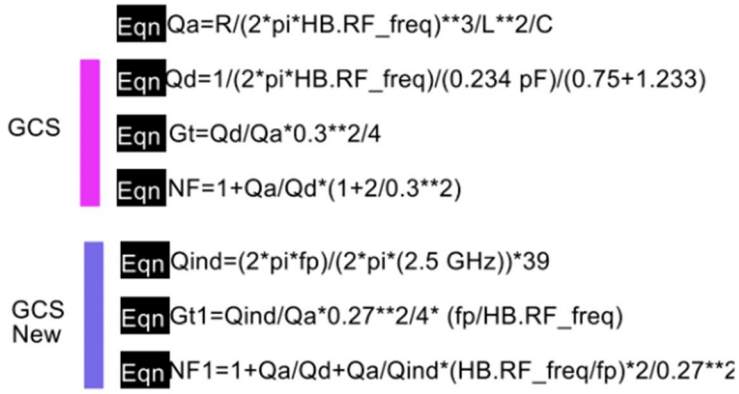

Fig 3.4.6 Original gain and NF equations vs. modified equations

In the figure, a new set of equations is adopted for calculating the gain and noise figure for the parametric amplifier. These equations are identical to the equations proposed by Hedayati, M. [2], with the additional introduction of the limitation from the resonance inductance Q. From the modified equations, the actual gain and noise figure are expected to be lower.

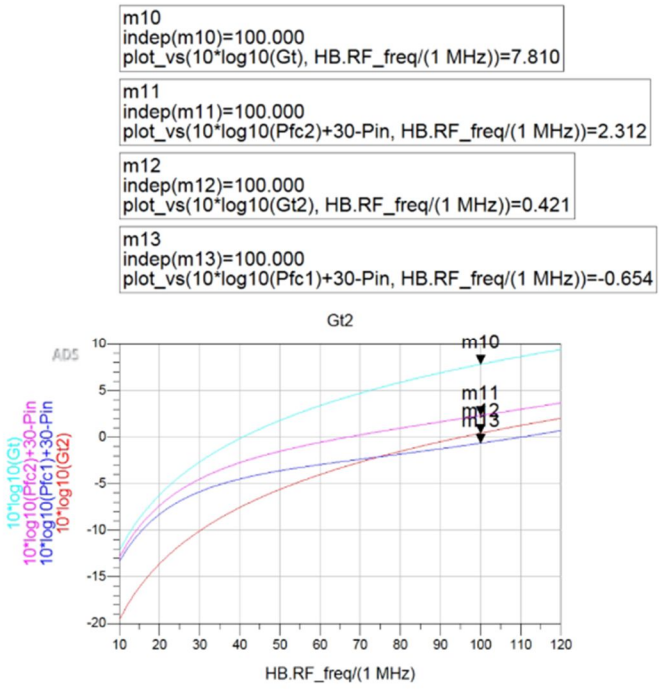

Fig 3.4.7 Adjusted Gain simulation results with comparison to the theoretical expectation

In Figure 3.4.7, the double sideband gain simulation result is presented along with results from the two methods of theoretical derivations. Starting from the original method, the result above presents us with a gain of 7.81 dB at 100 MHz, as shown in the light blue curve. On the other hand, the modified theoretical result presents us with a gain of 0.412 dB, as demonstrated by the red curve. The simulation shows results from both sidebands, in which the upper sideband has a gain of 2.312 dB, shown in the purple curve, and the lower sideband has a gain of -0.654 dB, shown in the blue curve.

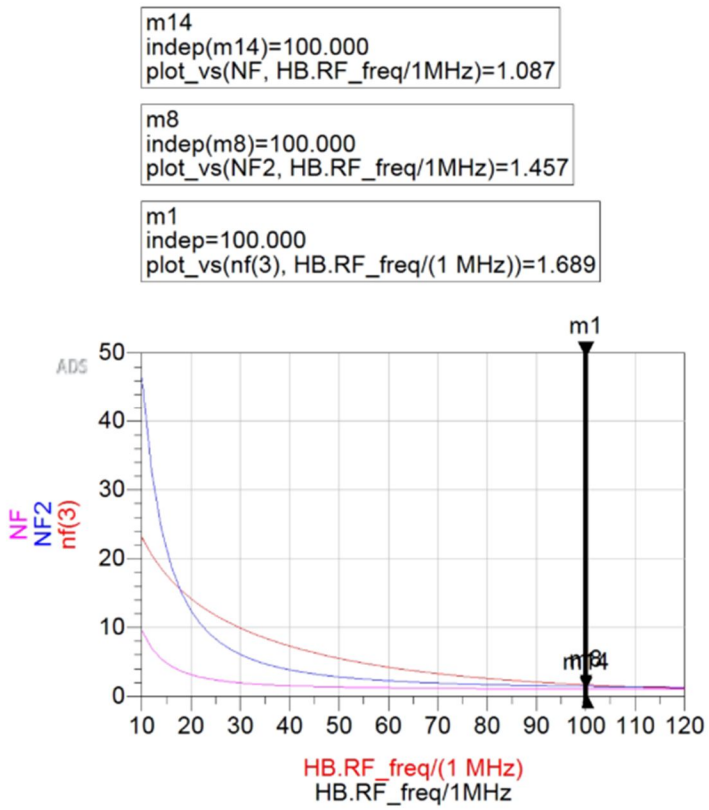

Fig 3.4.8 Adjusted NF simulation results with comparison to the theoretical expectations

In Figure 3.4.8, the blue curve represents the noise figure calculated using the new method with a value of 1.457 dB at 100 MHz. The purple curve represents the theoretical result calculated using the original derivation method. At 100 MHz, it has a noise figure of 1.087 dB. The red curve represents the simulated result, and at 100 MHz, it has a noise figure of 1.689 dB. According to this simulation, the consistency between modified equations and simulated results remains in both gain and noise figure, showing the effect of the limitation from the quality factor of the resonating inductor, and proving that the design is low noise and has sufficient double sideband gain.

CHAPTER 4

Solutions to Signal and Pump Noise in Parametric Receiver Design

4.1 Noise Floor Characterization

In the HF/VHF bands, antennas are subjected to several primary noise sources: the ambient environmental noise received by the antenna, the thermal noise generated by the antenna due to inherent losses, and the noise introduced by the matching network, if one is utilized. In addition, environmental noise originates from various radiation sources, often exceeding thermal radiation by 20 to 40 dB at HF. However, for the discussion in this section, a thermal equilibrium assumption is made, wherein the environment, the antenna, and the matching network are all at room temperature, and only thermal radiation is considered background noise. This assumption serves to simplify the analysis. Nevertheless, higher background noise levels can be incorporated subsequently once the receiver's noise performance under thermal equilibrium conditions is established. Thus, to analyze a device's noise figure, one needs first to understand the definition of thermal noise and define the noise floor. Based on fundamental thermodynamics, H. Nyquist showed that any two-terminal network under thermal equilibrium can be modeled by a noiseless resistor in series with a voltage noise source or shunt with a current noise source [11]. By referring to Figure 2.3.1 (a), e_n is given by.

$$\overline{e_n^2} = 4kTRp(f)B \tag{4.1.1}$$

Where k represents the Boltzmann constant and $p(f)$ is the Planck factor, and h is the Planck's constant.

$$p(f) = \frac{hf}{kT}\left(e^{\frac{hf}{kT}} - 1\right)^{-1} \tag{4.1.2}$$

The Planck factor is adopted for the energy equation to converge at higher frequencies (sub-mmwave). Here, in our frequency range of interest, we can further simplify equation 2.3.1 to the following:

$$\overline{e_n^2} = 4kTRB \tag{4.1.3}$$

Similarly, for the shunt case,

$$\overline{\imath_n^2} = \frac{4kTB}{R} \tag{4.1.4}$$

For a generator of internal resistance R_g, the noise power is calculated:

$$N_0 = \frac{\overline{e_n^2}}{R_{tot}} = \frac{4kTB}{\left(R_g + R_l\right)} = kTB \tag{4.1.5}$$

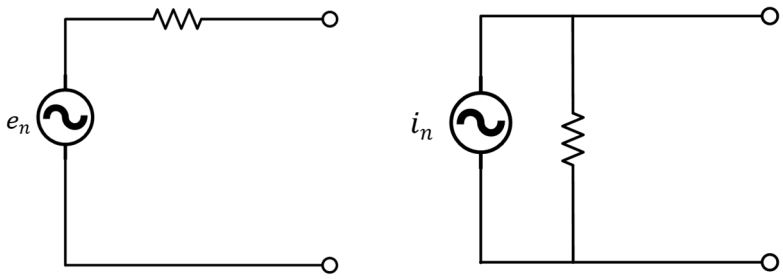

Fig 4.1.1 (a) Equivalent series representation for the noise power calculation, (b) shunt representation for the noise power calculation.

After defining the thermal noise floor, we can analyze various factors that introduce noise into the idler and pump port and their corresponding solutions.

4.2 Noise Collected from the Signal Band

During the preliminary studies of the supply noise introduced in the next section, we discovered that the noise in the FM radio frequency ranging from 88 MHz to 108 MHz persists in the signal frequency of 100 MHz. A possible solution to the problem is to migrate the signal frequency from 100 MHz to 80 MHz. The reference self-resonating meander line bowtie antenna is first revised to resonate at 80 MHz to further analyze the feasibility of this approach in the future.

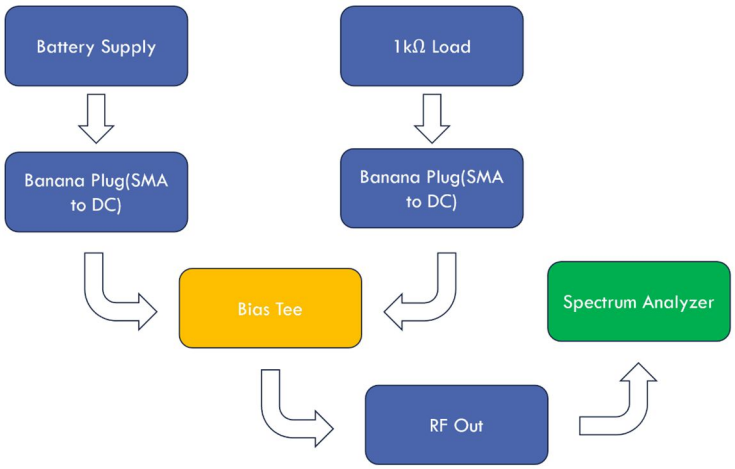

Figure 4.2.1 Original noise measurement flow chart for comparison of the DC power supply and the battery supply

In Figure 4.2.1, the original attempt, which compares the noise performance between the DC power supply and the battery supply, utilizes the bias tee to detect any noise while the supplies are driving a $1k\Omega$ load. Banana plugs convert DC to SMA connections. The RF output is connected to the spectrum analyzer to show the noise captured.

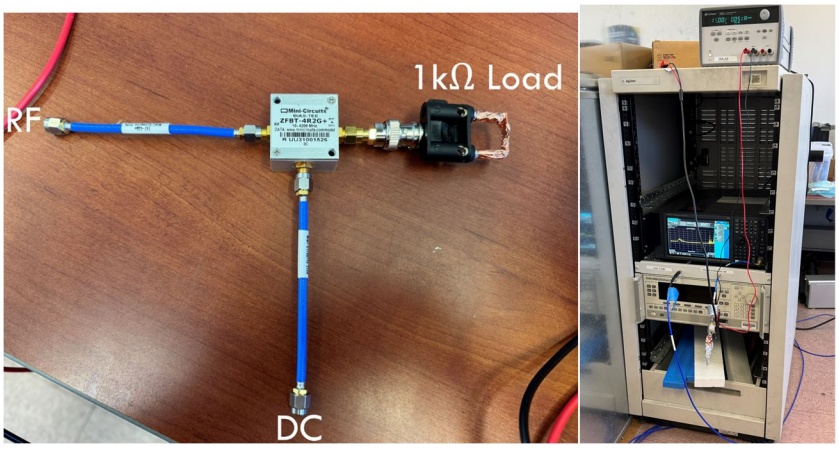

Figure 4.2.2 (a)Bias Tee setup, (b) Measurement setup with an additional LNA

Figure 4.2.2 shows the bias tee setup in (a). The $1k\Omega$ load is successfully connected to the banana plug through copper tapes. Such setup unintentionally made the banana plug and resistor pair a tiny loop antenna that is picking up noise from 83 MHz to 100 MHz as shown in the result below.

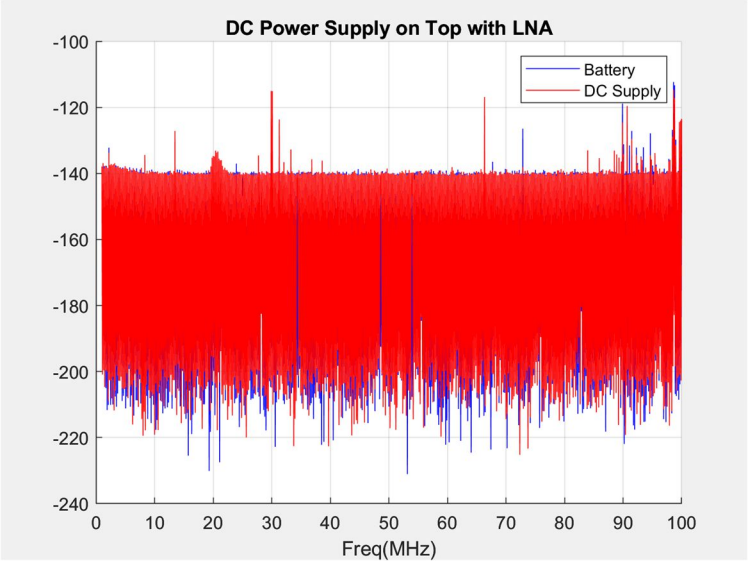

Fig 4.2.3 Overlay view for the noise performance of the battery supply and the Keysight DC Power supply at 5V bias

Figure 4.2.3 provides an overlay view of the noise performance between the battery supply and the Keysight DC power supply, showing low noise performance under the FM radio frequency. Since the frequency band is intrinsically noisy, some concerns are raised regarding noising coupling into the signal frequency for the receiving antenna. To address this problem, we redesign the reference meander line dipole antenna from self-resonating at 100 MHz to 80 MHz. The antenna is modified from the previous structure from peers while preserving the dipole length.

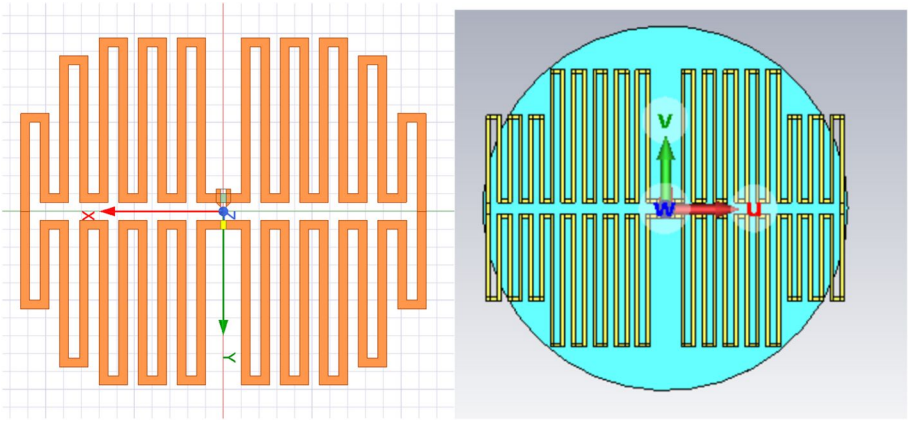

Fig 4.2.4 (a) original meander line dipole antenna (b) modified dipole antenna

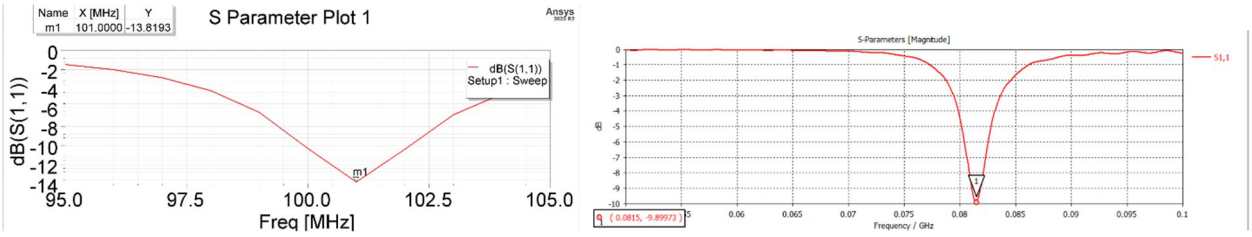

Fig 4.2.5 (a) S(1,1) simulation of the original antenna, (b) S(1,1) simulation of the modified antenna

Figure 4.2.4 presents the original meander line dipole antenna and the modified dipole antenna. The results shown in Figure 4.2.5 demonstrate that the original dipole resonates at 100 MHz, and the modified dipole resonates at 80 MHz. The modified dipole decreases its linewidth to accommodate more turns needed to lower the resonance frequency. The metal thickness for both

antennas is 35 um. The substrate material uses FR-4 with ϵ of 4.3 and μ of 1. The diameter of the substrate plate remained at 590 mm for both antennas. Differential feeding is defined at the antenna port.

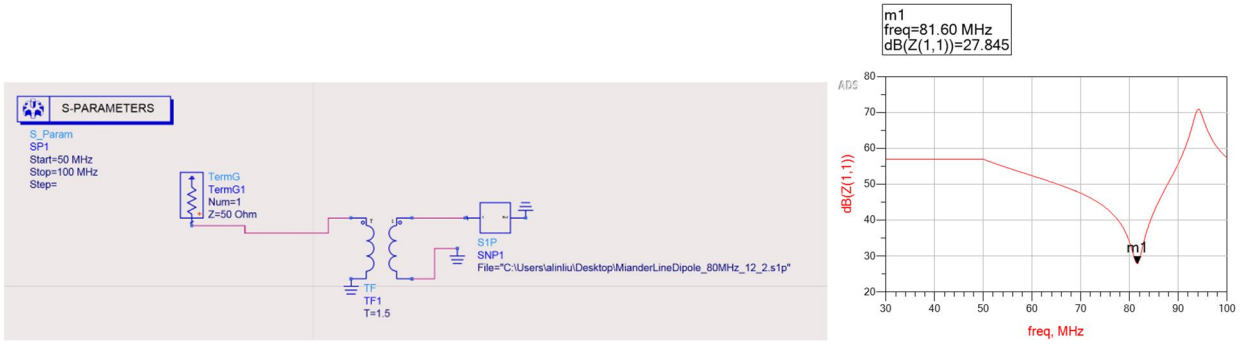

Fig 4.2.6 (a) Exported touchstone of the modified dipole antenna (b) antenna impedance at the resonance with T = 1

The transformation ratio T is defined as $\left(\frac{N_2}{N_1}\right)$, the ratio of the number of turns in the secondary coil to the number of turns in the primary coil. The impedance transformation is characterized using the following equation:

$$\left(\frac{Z_2}{Z_1}\right) = \left(\frac{N_2}{N_1}\right)^2 = T^2 \tag{4.2.1}$$

In Figure 4.2.6, the transformation ratio is chosen to be 1.5 to transform the antenna impedance of 27.845 Ω to 60.75 Ω for better matching. Though the characteristic impedance is set to be 50 Ω at the input, the transformed impedance is already sufficient to keep the antenna S(1,1) beneath -20 dB, indicating low return loss at the resonance. The S(1,1) performance is validated in Figure 4.2.7.

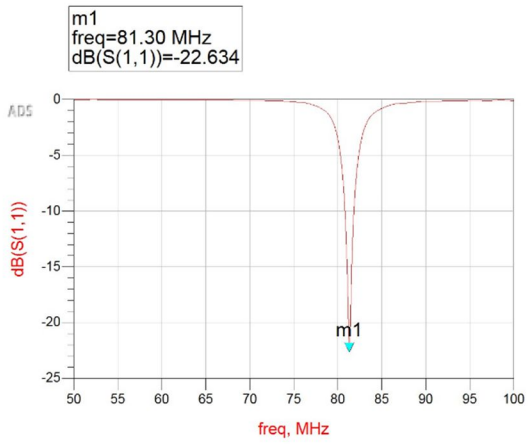

Fig 4.2.7 S(1,1) simulation with T = 1.5

Then, the ideal transformer is replaced with the extracted S-parameter model of a commercially available transformer with an impedance transformation ratio of 2, allowing the original antenna impedance of 27.8 Ω to be transformed to 55.6 Ω. The setup and result are shown in Figure 4.2.8.

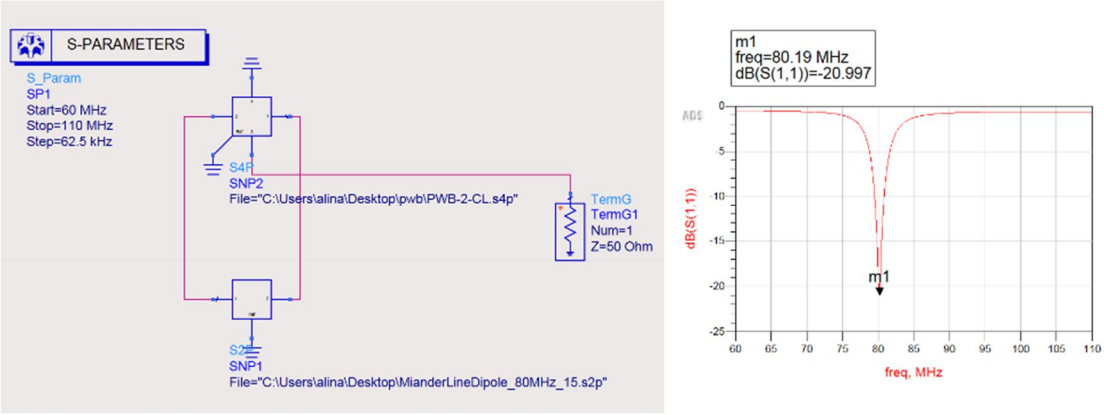

Fig 4.2.8 (a) Simulation setup with PWB-2-CL S4P (b) S-parameter of the impedance transformed dipole antenna

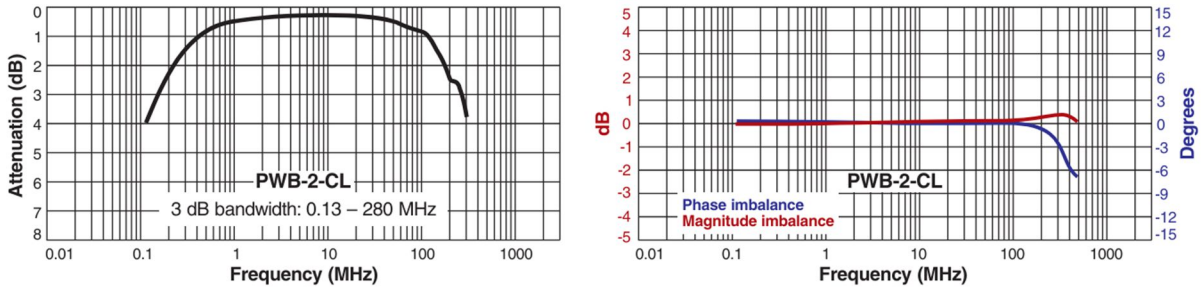

Fig 4.2.9 Transformer attenuation and phase imbalance from the component datasheet

In Figure 4.2.9, the transformer attenuation and phase imbalance are shown. The transformer has a low attenuation value of 0.8 dB, and a phase imbalance of 0 dB at 80 MHz, serving as an excellent device for building the actual impedance transformation network. Next, the antenna is fabricated by an outside foundry. The transformer is soldered to an PCB design, featuring pads and vias for a SMP connector, and differential feeding of the antenna shown in Figure 4.2.10.

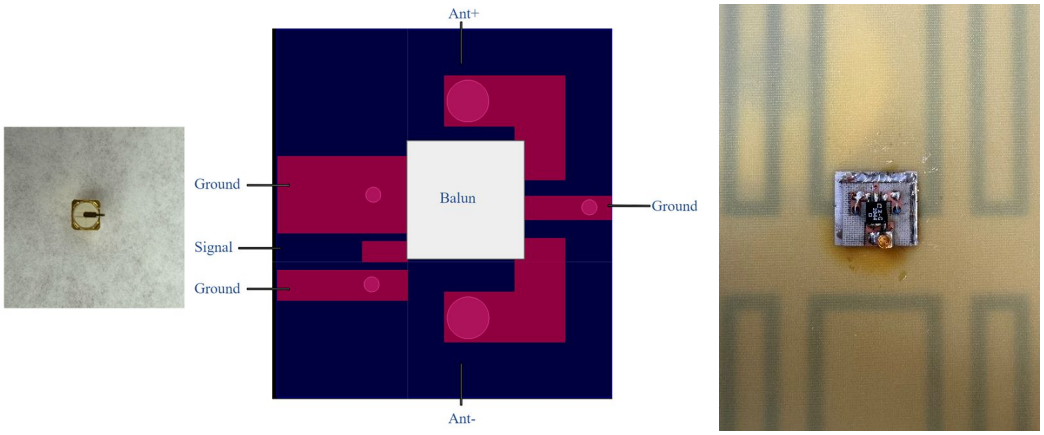

Fig 4.2.10 (a) PCB design for impedance transformation network and antenna feeding (b) mounted view of the PCB design

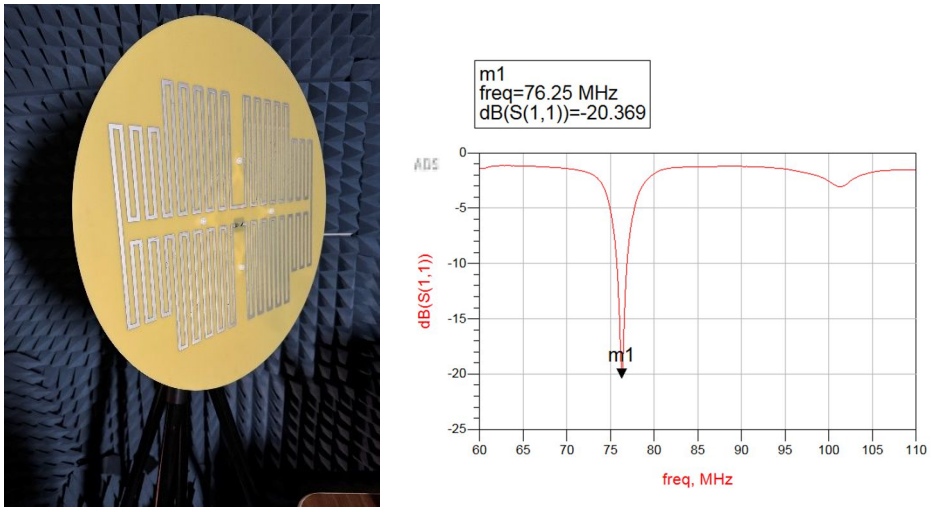

Fig 4.2.11 (a) Antenna chamber measurement setup (b) S-parameter result

In figure 4.2.11, the antenna S-parameter is measured in the chamber with the PCB directly mounted on the back. The measured S(1,1) result is presented on the right, and the result is transformed from differential to single-ended via an ideal 3-port balun in ADS. With -20.369 dB at the resonance frequency, the antenna is well matched for future use of noise analysis at 80 MHz.

4.3 Supply Noise

Standard methods of supplying DC voltages towards components, such as LNA, filters, and the pump, use devices like Keysight Agilent DC power supplies. The measurement environment for ESAs operating at the HF and VHF range usually requires the chamber walls to be at least $\lambda/2$ away from the antenna under test (AUT). Thus, AC to DC cables of several meters in length are utilized to bias the pump, LNA, and mixers. Hence, the cable attenuation becomes a significant factor in noise measurement and analysis. In addition, cables of such length will also operate as a monopole that picks up noise at hundreds of MHz range or below. The noise enters the pump and

gets upconverted to the idler frequencies, distorting output signals. Thus, in the real-life setup for this project, any power supply far away from the physical antenna shall be replaced by battery supplies built with the LDO eval boards or compact variable AC to DC converters extended with DC cables for LNAs that need large power consumption.

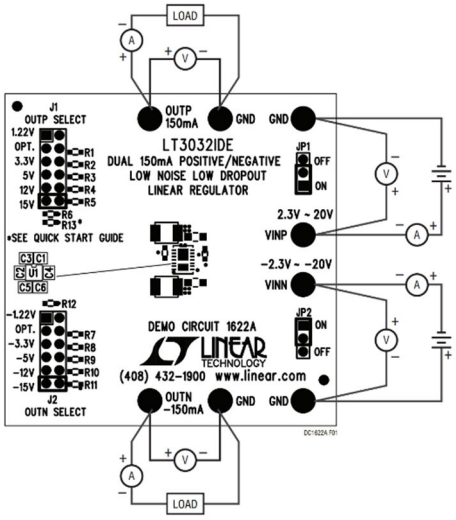

Fig 4.3.1 (a) DC1622A eval board with LT3032IDE dual, positive and negative low dropout linear regulator that converts $\pm 9V$ battery input to $\pm 5V$ for the pump,

In Figure 4.3.1, a DC1622A eval board with LT3032IDE low dropout linear regulator is presented. The low noise characteristics of $20u\ V_{RMS}$ (positive regulator) and $30u\ V_{RMS}$ (negative regulator) over a 10 Hz to 100kHz bandwidth, which is ignorable compared to the thermal noise.

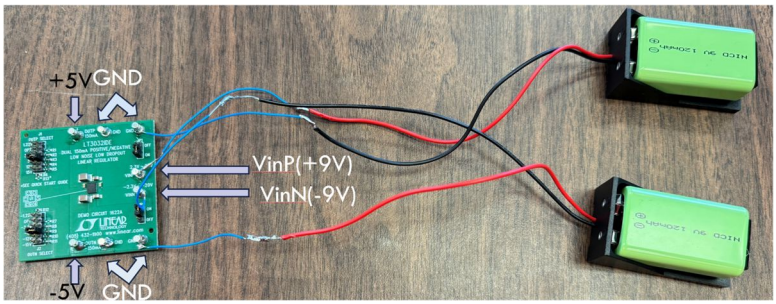

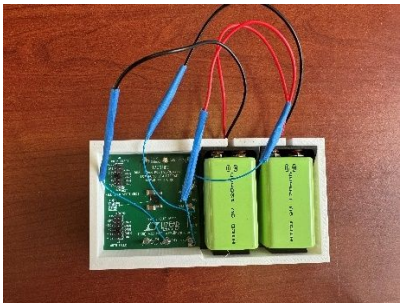

Fig 4.3.2 (a) Complete battery supply setup, (b) Battery housing for testing

In Figure 4.3.2 the complete setup is shown with $\pm 9V$ as input to the LDO and generate a $\pm 5V$ as output. The eval board can support up to 150 mA of current which is more than sufficient for the pump biasing under 2 mA. The battery housing is designed and constructed to ensure the connections are in place, and it becomes more compacted for future assembly.

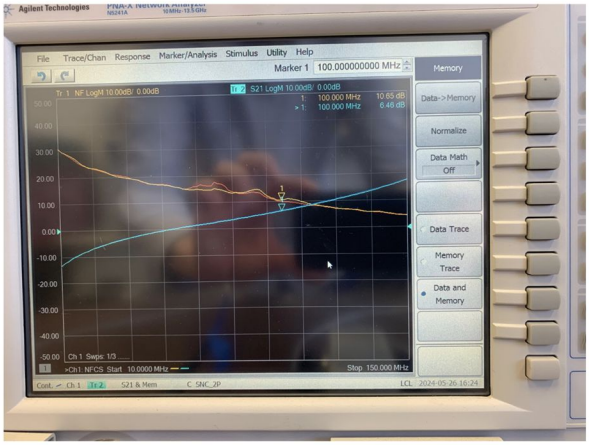

Fig 4.3.3 Measured noise figure performance in comparison to standard Keysight power supply at the pump

In Figure 4.3.3, the measurement result is shown by comparing performance using the standard Keysight power supply to the one with the battery supply. These supplies are used to bias the pump of the amplifier at 5V. The parametric receiver is measured in the chamber, and the YIG filter introduced in section 4.4 is also utilized to filter out synthesizer noise at the pump. From the results above, we can see that by using the battery supply or DC power supply in indoor testing, noise figure from both cases are almost identical, indicating that no additional noise is introduced, but the battery supply option still avoids cable noise and attenuation for ESA measurement in the outdoor settings for HF and VHF range.

4.4 Pump Noise Filtration

In practice, the synthesizer built-in noise often exceeds the thermal noise floor by 10 to 20 dB, and the noise at idler frequencies enters through the pump port and leaks directly to the idler output. Thus, a YIG filter is proposed as a solution to filter out the synthesizer noise and reveal the actual thermal noise floor. Figure 4.4.1 shows the setup to verify the dominance of the true noise floor over the synthesizer noise floor. The thermal noise floor is calculated and defined in section 4.1. At room temperature, the thermal noise is -174 dBm/Hz. The signal synthesizer has some built-in noise that would significantly affect the accuracy of the measurement. Thus, in Figure 4.2.1, an LNA is added to the front of the spectrum analyzer to dominate such noise and show the observer a true noise floor. For example, according to equation (4.1.5), the thermal noise floor shall be -174 dBm/Hz, and with an LNA of 30 dB gain, the true noise floor is now raised to -144 dBm/Hz. The common synthesizer noise floor is usually around -155 dBm/Hz. By adding the LNA in the front, the front-end noise now dominates, and the true noise floor can be revealed.

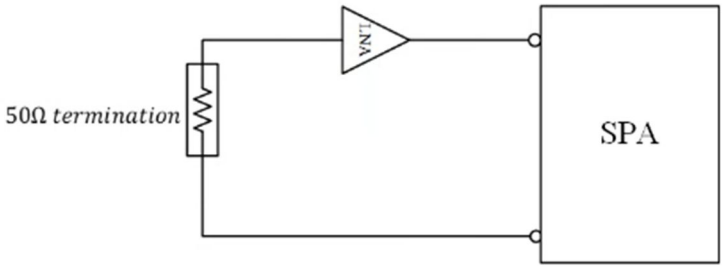

Fig 4.4.1 Setup for noise floor dominance

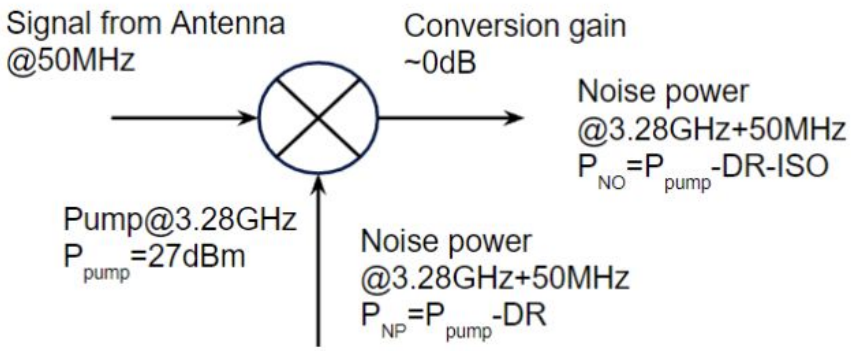

Fig 4.4.2 Noise power calculation and parametric amplification illustration

Figure 4.4.2 shows calculations for the noise power entering through the pump and the noise power appearing at the idler output. The signal synthesizer generates a signal output of 0 dBm, which is amplified with an LNA of 27 dB gain and a 3 dB noise figure. The synthesizer's minimum noise floor is at -155 dBm/Hz. According to the equation (4.4.1), the synthesizer's dynamic range is 155 dB.

$$DR = 0\ dBm - minimum\ noise\ floor \tag{4.4.1}$$

$$P_{NP} = P_{pump} - DR + NF \tag{4.4.2}$$

$$P_{No} = P_{NP} - ISO \tag{4.4.3}$$

The noise power at the pump port is represented by P_{NP}, and the noise power at the idler port is represented by P_{No}. Isolation between the pump port and the idler port is represented by ISO. Both the LNA and synthesizer noise at the idler frequency get amplified and leak directly to the idler port. The combination of the parametric amplifier chip with couplers can typically provide isolation of around 27 dB and the pump power of 27 dBm above, the equation (4.4.2) yields a P_{NP} of -125 dBm/Hz.

$$P_{NP} = P_{pump} - DR \tag{4.4.2}$$

The noise power at the idler port is defined as:

$$P_{No} = P_{NP} - ISO \tag{4.4.3}$$

In this example, using equation (4.4.3), the noise power at the idler is $P_{No} = -125\ dBm/Hz - 27dB = -152\ dBm/Hz$. The value is 22 dB higher than the thermal noise floor. To tackle the pump noise leakage problem, a YIG filter is proposed to be added at the pump port to filter out the noise at idler frequencies, avoiding noise leakage from the pump port to the idler port. Thus, a de-embedding circuit is designed to characterize the noise through the YIG filter before adding it to the receiver chain. The procedure is introduced in the figure below.

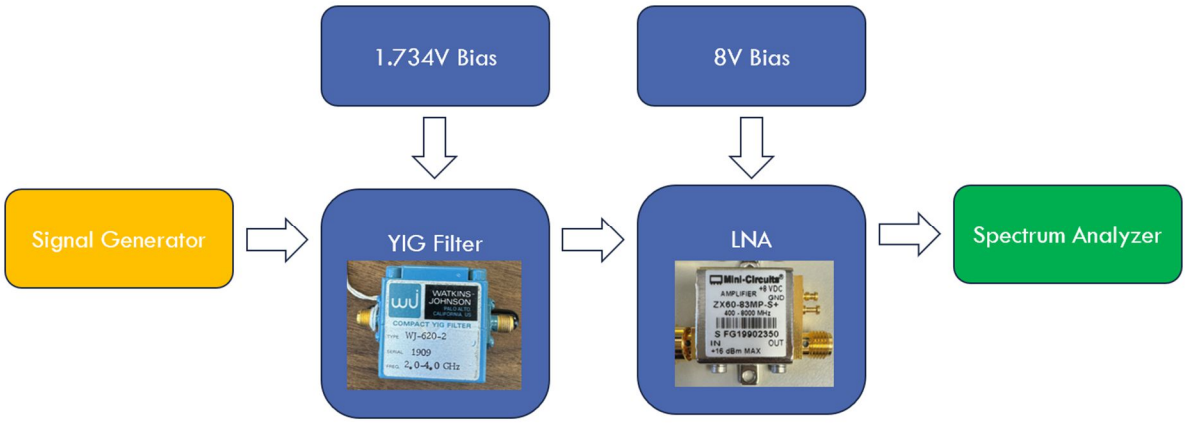

Fig 4.4.3 Flow chart for de-embedding the noise from the YIG filter

In Figure 4.4.3, the WJ-620-2 YIG filter from Watkins-Johnson Company is measured with RF signal input using a signal generator, and the output of the filter is amplified by the LNA ZX60-83MP-s+ with a gain of 20 dB. The noise coming through the entire RF path is captured by the spectrum analyzer. YIG filters are band-pass filters with frequency tunability controlled by the DC bias voltage. A 1.734 V sets the passband center frequency at 3.28 GHz. YIG filter's narrow

bandwidth characteristics work in our best interest, as after implementation of the filter in the receiver chain, we would like it only to allow the pump signal to go through while rejecting all the out-of-band noise.

Fig 4.4.4 Signal output at the center frequency of 3.28 GHz with 15 $\boldsymbol{dBm}$ RF input and 34 dB machine attenuation

In Figure 4.4.4, we measure the signal output and noise floor at room temperature, with 10 kHz bandwidth, and the LNA gain is 20 dB. An input RF power of 15 dBm is supplied, and a signal output of 26.5 dBm is achieved, and a 34 dB machine attenuation is added to protect the spectrum analyzer. With the machine attenuation, the noise floor measurement becomes invalid because noise entering the designated sideband frequency ($f_c \pm f_s$) also gets attenuated.

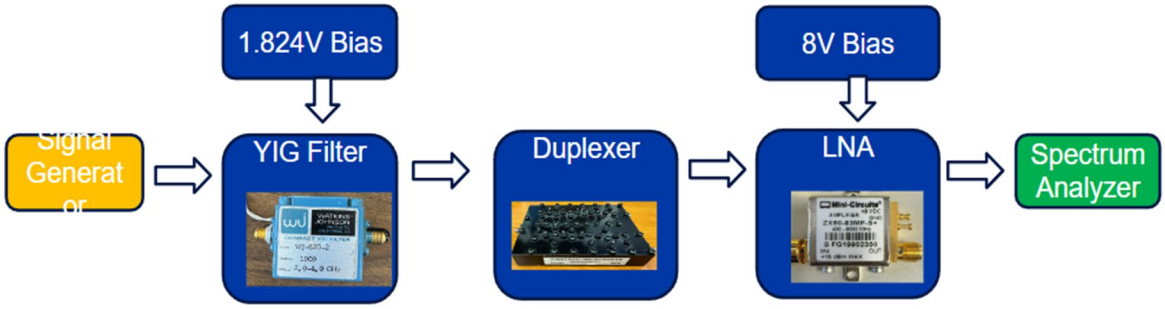

Fig 4.4.5 Flow chart for de-embedding the noise from the YIG filter with duplexer

In Figure 4.4.5, the duplexer consists of two bandpass filters with high out-of-band rejection and fixed center frequencies. Only one of the filters is needed for our testing purposes.

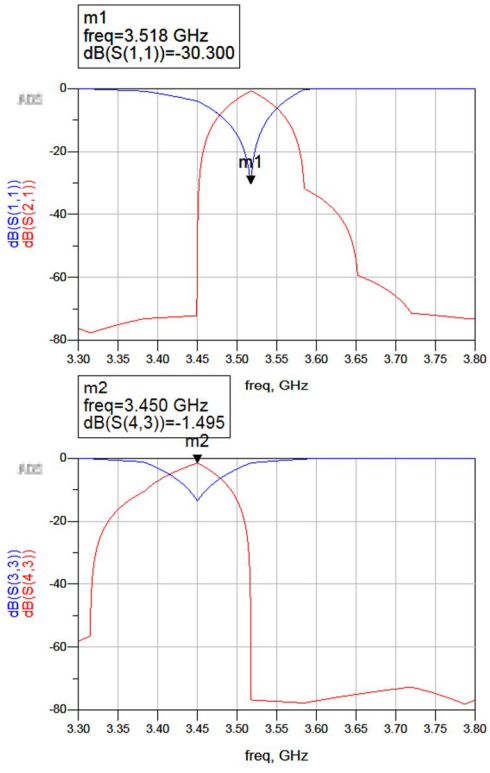

Fig 4.4.6 S(2,1) and S(1,1) measurements of the transmitter and receiver path of the duplexer

In Figure 4.4.6, the S-parameter measurements of the two bandpass filters are measured separately, with the top one being the Tx path and the bottom one being the Rx path. The Tx path was chosen for the purpose of our design due to its lower return loss in the "noise band" shown in the figure below. In Figure 4.4.7, it shows how the RF input signal, and the YIG filter center frequency falls out of the pass band of the duplexer, allowing the RF input signal to be attenuated while the noise through the YIG filter gets preserved and then amplified through the LNA. With the noise band ranging from 3.45 to 3.58 GHz, we choose the signal and YIG filter center frequency at 3.43 GHz, corresponding to a DC bias of 1.824 V for the YIG filter.

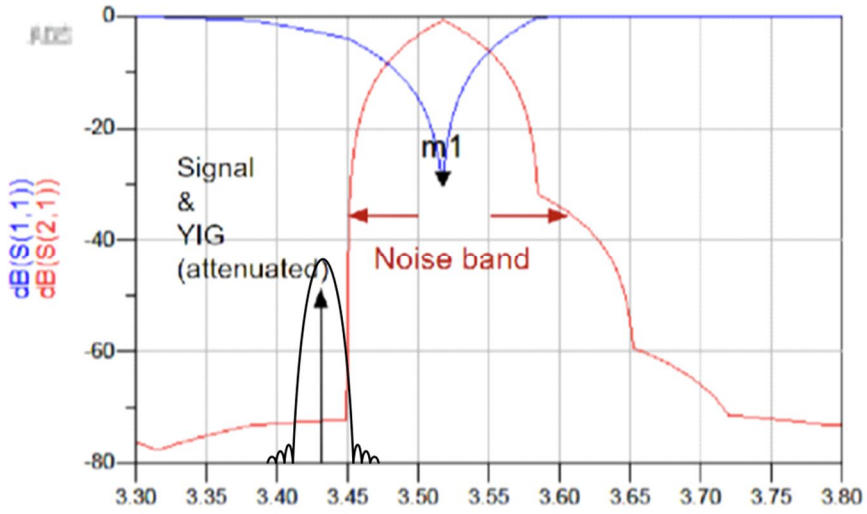

Fig 4.4.7 Diplexer performance and function

Fig 4.4.8 Noise floor validation

The first step of the test is to verify the true noise floor in the measurement. The validation follows the circuitry shown in Figure 4.4.1. From equation (4.1.5), with a 10 kHz resolution and an LNA gain of 20, the theoretical noise floor level is at -114 dBm. From Figure 4.4.8, the result shows that the measured noise floor is at around -111.89 dBm, showing consistency between the measurement and theory. After validating the noise floor, we can proceed with the setup shown in Figure 4.4.8, which was discussed in the previous paragraphs. From the measurement results shown in Figure 4.4.9, we can perceive that the noise floor level remains at around -112 dBm regardless of the RF input power level, while the RF input signal is successfully attenuated. Thus, the YIG filter effectively suppresses the synthesizer noise without introducing additional noise and it shall serve as a qualified candidate for eliminating the noise entering through the pump port.

Fig 4.4.9 (a) RF input power at 0 $\boldsymbol{dBm}$ (b) RF input power at 10 $\boldsymbol{dBm}$

CHAPTER 5

Conclusion and Future Work

In conclusion, this work demonstrates the importance of noise analysis in parametric receiver design and characterizes the noise at the signal and pump ports. It successfully proved the excellence of parametric amplifier for its low noise, easy to design characteristics while still providing adequate double side band gains. With the help of external devices, such as filters and couplers, we conclude that the parametric amplifier can be used to address and overcome the conventional bandwidth-efficiency limit of electrically small antennas. With that said, more work needs to be done when it comes to leakage cancellation of the amplifiers. Future work includes the physical realization of prototypes with better balun performance for MMIC design or cooperating with the on-chip prototype with off-chip high Q external components.

References

[1] Y. E. Wang, "Theory of Broadband Noise Matching for HF/VHF Receivers With Electrically Small Antennas," in IEEE Access, vol. 11, pp. 56574-56592, 2023, doi: 10.1109/ACCESS.2023.3282178.

[2] Hedayati, M. (2022). “Parametronics”- A New Way to Design Low Noise High Efficiency RF Microwave Front Ends. UCLA. ProQuest ID: Hedayati_ucla_0031D_21257. Merritt ID: ark:/13030/m5hf54hs. Retrieved from https://escholarship.org/uc/item/7zr3x25t

[3] L. J. Chu, “Physical limitations of omni‐directional antennas,” J. Appl. Phys., vol. 19, no. 12, pp. 1163–1175, 1948.

[4] H. A. Wheeler, “Fundamental limitations of small antennas,” Proc. IRE, vol. 35, no. 12, pp. 1479–1484, 1947.

[5] R. M. Fano, “Theoretical limitations on the broadband matching of arbitrary impedances,” J. Franklin Inst., vol. 249, no. 1, pp. 57–83, 1950.

[6] P. Loghmannia and M. Manteghi, “An active cavity-backed slot antenna based on a parametric amplifier,” IEEE Trans. Antennas Propag., vol. 67, no. 10, pp. 6325–6333, 2019.

[7] H. Li, A. Mekawy, and A. Alù, “Beyond Chu’s limit with Floquet impedance matching,” Phys. Rev. Lett., vol. 123, no. 16, p. 164102, 2019.

[8] P. Loghmannia and M. Manteghi, “Broadband parametric impedance matching for small antennas using the Bode-Fano limit,” IEEE Antennas and Propagation Magazine, pp.2-15, July, 2021.

[9] K. Q. T. Luong, W. Gu, F. Fereidoony, L. Yeung, Z. Yao, and Y. E. Wang, “Radio Frequency Precession Modulation Based Magnetic Field Sensors,” IEEE Access, 2022.

[10] J. M. Manley and H. E. Rowe, “Some general properties of nonlinear elements-Part I. General energy relations,” Proc. IRE, vol. 44, no. 7, pp. 904–913, 1956.

[11] L. A. Blackwell and K. L. Kotzebue, *Semiconductor-Diode Parametric Amplifiers*. Englewood Cliffs, N.J: Prentice-Hall, 1961.